ACS APPLIED MATERIALS & INTERFACES

Research Article

www.acsami.org

Ti_3C_2 MXene as a High Capacity Electrode Material for Metal (Li, Na, K, Ca) Ion Batteries

Dequan Er,[†] Junwen Li,[†] Michael Naguib,[‡] Yury Gogotsi,[‡] and Vivek B. Shenoy*[,†]

[†]Department of Materials Science and Engineering, University of Pennsylvania, Philadelphia, Pennsylvania 19104, United States

[‡]Department of Materials Science and Engineering and A.J. Drexel Nanomaterials Institute, Drexel University, Philadelphia, Pennsylvania 19104, United States

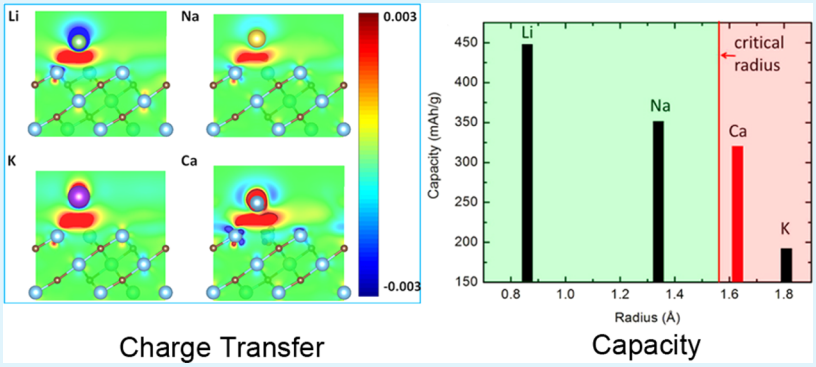

ABSTRACT: Two-dimensional (2-D) materials are capable of handling high rates of charge in batteries since metal ions do not need to diffuse in a 3-D lattice structure. However, graphene, which is the most well-studied 2-D material, is known to have no Li capacity. Here, adsorption of Li, as well as Na, K, and Ca, on Ti_3C_2, one representative MXene, is predicted by first-principles density functional calculations. In our study, we observed that these alkali atoms exhibit different adsorption energies depending on the coverage. The adsorption energies of Na, K, and Ca decrease as coverage increases, while Li shows little sensitivity to variance in coverage. This observed relationship between adsorption energies and coverage of alkali ions on Ti_3C_2 can be explained by their effective ionic radii. A larger effective ionic radius increases interaction between alkali atoms, thus lower coverage is obtained. Our calculated capacities for Li, Na, K, and Ca on Ti_3C_2 are 447.8, 351.8, 191.8, and 319.8 mAh/g, respectively. Compared to materials currently used in high-rate Li and Na ion battery anodes, MXene shows promise in increasing overall battery performance.

KEYWORDS: *Ti_3C_2, alkali ions, charge transfer, capacity, electrode, battery, MXene*

1. INTRODUCTION

Energy storage systems have powered the world of technology. Their applications vary from portable electronic devices and electric vehicles, to large scale power grid systems that are needed to manage intermittent renewable energy supplies. Among different energy storage systems, batteries have several advantages such as their compact size and their high efficiency.[1,2] More specifically, lithium-ion batteries (LIBs) have attracted most attention since their first commercialization by Sony in 1991, because of their high energy density and wide voltage window. However, the development of LIBs has been hindered by safety and cost issues,[3] and the currently used materials operate close to their theoretical limit. Therefore, batteries utilizing other metal ions are needed. In addition, with the current growth rate of LIB use in electric vehicles and grid-level storage systems, Li scarcity can be a future problem. Since sodium is more abundant and cheaper than lithium, Na-ion batteries (NIBs) can be a good candidate to replace LIBs in the future.[4,5] In addition to NIBs, other alkali ions such as potassium have been found promising.[6] Multivalent ions, such as aluminum, magnesium, and calcium may offer higher energy density than monovalent Li, if two or three electrons can transfer per ion. However, in most of the nonconventional metal ion batteries described above, more improvements are still needed in order for them to get to real world applications. Most of the challenging questions involve the optimum electrolyte for each system and finding host materials to work as electrodes. Graphite, which is a successful anode for LIBs, cannot be used in NIBs, because the Na−C interaction is found to be too weak to contribute to the necessary Coulomb interactions.[7]

Two-dimensional (2-D) materials are of special interest as host materials for metal ion batteries, due to their unique morphology, which enables fast ion diffusion and offers more ion insertion channels with the whole surface exposed.[8] Recently, a new family of 2-D early transition metal carbides

Received: February 24, 2014
Accepted: June 30, 2014
Published: June 30, 2014

and carbonitrides, so-called "MXenes", was synthesized by selective etching of A atoms from MAX phases with hydrofluoric acid (HF) at room temperature.[9,10] The MAX phase is a large family (+60 phases) of ternary metal carbides with composition of $M_{n+1}AX_n$, where M is an early transition metal, A is one of the group A elements, X is carbon and/or nitrogen, and n can be 1, 2, or 3.[11] To date, the following MXenes have been synthesized experimentally: Ti_3C_2,[10] Ti_2C, $(Ti_{0.5}Nb_{0.5})_2C$, Ta_4C_3, $(V_{0.5}Cr_{0.5})_3C_2$, Ti_3CN,[9] V_2C, and Nb_2C.[12] Since their discovery, MXenes have attracted great attention and have displayed interesting properties. For example, the conductivity of multilayered MXenes was found comparable to that of multilayered graphene.[9] Theoretical studies[13−16] regarding different properties also began soon after the experimental discovery of MXene systems. Shein and Ivanovskii[13,14] have studied the structural features and relative stabilities of the MXene $Ti_{n+1}C_n$ and $Ti_{n+1}N_n$ (n = 1,2,3). Density functional theory (DFT) calculations showed that MXenes can be semiconductors with tunable band gap that can be controlled by changing the surface termination,[10,17] but nonterminated MXenes are metallic and are expected to have the highest conductivity.[18] Kurtoglu et al.[19] have estimated the in-plane elastic constants of MXenes, using DFT, to be more than 500 GPa, which means that MXenes are expected to have higher stiffness than structural steel (400 GPa).

MXenes have been found to be promising electrode materials for LIBs[20,21] and lithium ion capacitors.[22] Although the capacity of MXenes for Li is close to that of commercial graphite electrodes in LIBs (372 mAh/g), MXenes have shown an excellent capability to handle high cycling rates. For example, at a cycling rate of 36 C, a reversible capacity of 110 mAh/g was obtained for additive-free terminated Ti_3C_2.[21] Note that graphite cannot handle such high cycling rates. This may be attributed to the smaller diffusion barrier for Li atoms on Ti_3C_2. Using DFT calculations, Shen et al.[23] found that the diffusion barrier of Li atoms on Ti_3C_2 (0.07 eV) is smaller than that in anatase TiO_2 (0.35−0.65 eV) and graphite. However, studies of electronic properties and applications of MXenes are needed to utilize other metal ions in batteries. No experimental data for NIBs or other metal ion batteries with MXene electrode have been reported to date. In this work, we choose Ti_3C_2 as the representative and best studied MXene and report on its performance as an electrode material for different metals (Li, Na, K, and Ca) ion batteries using first-principles DFT calculations.

2. METHODOLOGY

All our calculations were performed using the Vienna ab initio simulation package (VASP)[24] with the projector augmented wave (PAW)[25,26] potentials for core electrons and the Perdew−Burke−Ernzerhof (PBE)[27] form of the generalized gradient approximation (GGA) for exchange and correlation functional. An energy cutoff of 650 eV was used for the plane wave expansion of valence electron wave functions. The Brillouin zone was sampled using a Monkhorst−Pack special k-point mesh of Γ-centered 12 × 12 × 1 for the unit cell of Ti_3C_2. To simulate the adsorption of single Li, Na, K, and Ca, we used a 3 × 3 × 1 supercell, corresponding to the adatom content x = 1/9 in $Ti_3C_2M_x$. Higher adatom contents up to x = 2.0 were also investigated. To avoid interactions between simulated two-dimensional Ti_3C_2 monolayer sheet and the periodic images, a vacuum space larger than 10 Å was used. All structures were relaxed with all atoms allowed to move until the force on each atom was less than 0.05 eV/Å.

To obtain the open circuit voltage (OCV),[28] we considered the reaction

$$Ti_3C_2 + xM \rightarrow Ti_3C_2M_x \quad (1)$$

where x is the number of adatoms inserted in the unit cell of Ti_3C_2. The electronic potential during this process can be written in the form of Gibbs free energy

$$V = -\frac{\Delta G_f}{zF} \quad (2)$$

where z and F are the number of valence electrons during the adatom process and the Faraday constant, respectively; ΔG_f is the change in Gibbs free energy during the adatom process which is defined as

$$\Delta G_f = \Delta E_f + P\Delta V_f - T\Delta S_f \quad (3)$$

$P\Delta V_f$ is on the order of 10^{-5} eV and the term $T\Delta S_f$ is comparable to 26 meV at room temperature; thus, the entropy and pressure terms are negligible.[28] ΔG_f is then approximately equal to the formation energy, ΔE_f, involved in the adsorption process, which is defined as

$$\Delta E_f = E_{Ti_3C_2M_x} - (xE_M + E_{Ti_3C_2}) \quad (4)$$

where $E_{Ti_3C_2M_x}$ is the total energy of the composite system with x metal atoms adsorbed in the unit cell of Ti_3C_2, E_M is the total energy of a single Li, Na, or K atom in a bulk BCC structure or Ca in a bulk FCC structure, and $E_{Ti_3C_2}$ is the total energy of an isolated Ti_3C_2. The OCV is related to the formation energy by

$$OCV = \frac{\Delta G_f}{x} \approx -\frac{\Delta E_f}{x} \quad (5)$$

3. RESULTS AND DISCUSSION

3.1. Structure Models. By removing the Al atom from bulk Ti_3AlC_2, monolayer Ti_3C_2 is constructed with quintuple layers stacked in a sequence of Ti(s)−C−Ti(c)−C−Ti(s), where Ti(s) corresponds to the surface Ti atoms and Ti(c) corresponds to the center Ti atoms in Ti_3C_2. The relaxed structure was found to have a lattice constant a = 3.1005 Å, which is in good agreement with the experimental value 3.057 Å.[21] The structure can also be described as trilayer Ti-atomic layers being interleaved with two C atomic layers forming an edge-shared TiC_6 octahedral structure as shown in Figure 1. The unit cell of Ti_3C_2 is highlighted in a 3 × 3 × 1 supercell.

Here we only consider the adsorption on the surface of Ti_3C_2 MXene. It is easy to recognize the high symmetry adatom sites A, B, and C as indicated in Figure 1 on the surface: The A site is at the center of a hexagon composed of carbon atoms, the B site is directly above the carbon atom, and the C site is directly above the Ti atom. Compared to the surface adsorption, the insertion of metal ions into the inner interstitial site is energetically less favorable. We have performed calculations of bulk interstitial adsorption for Li, Na, K, and Ca. The adsorption energies are 4.40, 12.23, 15.39, and 12.21 eV, respectively. The disruption of structure integrity was also observed.

3.2. Adatom Adsorption. The binding of metal ions on Ti_3C_2 was studied by calculating the adsorption energy E_{ad} using larger super cell with x = 1/9 in $Ti_3C_2M_x$. Because E_{ad} = −OCV, the large positive OCV indicates energetically favorable

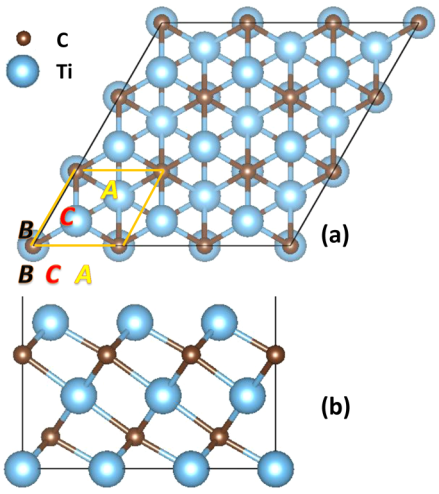

Figure 1. Schematic diagram showing the crystal structure of a Ti_3C_2 monolayer with (a) top and (b) side view. The large blue balls represent Ti atoms and small brown balls represent C atoms. The highlighted unit cell indicates the high symmetry *A*, *B*, and *C* adatom sites.

adsorption. In Table 1, we list the calculated OCVs for Li, Na, K, and Ca adatoms on *A*, *B*, and *C* sites. For all atoms, the OCV

Table 1. Energetic and Structural Properties of Li, Na, K, and Ca Adatoms on Ti_3C_2 Monolayer[a]

	OCV (eV)			q (e^-)		h (Å)	
	A	*B*	*C*	*A*	*B*	*A*	*B*
Li	0.43	0.43	0.30	0.21	0.19	2.51	2.50
Na	0.74	0.74	0.72	0.40	0.38	2.84	2.82
K	1.90	1.90	1.81	0.47	0.36	3.27	3.25
Ca	1.43	1.42	1.33	1.31	1.24	2.72	2.70

[a]OCV, Bader charge (q), and adatom height (h) of energetically favorable *A*, and *B* sites for Li, Na, K, and Ca on Ti_3C_2.

of *A* is close to that of *B* whereas that of *C* is lower. *A*- and *B*-site OCVs are higher than that of the *C* site by about 100 meV. The OCV of each site increases with the alkali atom mass, suggesting stronger adsorption for heavier alkali elements. However, this tread does not apply for Ca due to its different valence ($[Ar]4s^2$) electron configuration. In the following discussions, we focus on the adsorption of *A* and *B* sites sine the C sites are less energetically favored.

In addition to the OCVs, the adsorption strength of adatoms on different sites is also reflected in the adatom height h which is defined as the vertical distance between the adatom and the topmost surface Ti atom. The adatom heights for *A* and *B* sites are listed in Table 1. It can be seen that for *A* and *B* sites the adatoms have very close height, consistent with the comparable OCVs for these two sites. With the increase of element mass of alkali adatoms, h increases for both sites excluding Ca.

To gain deeper insight into the difference in adsorption for different metal atoms on Ti_3C_2, we performed the electronic structure calculations. Figure 2 (a), (b), (c), and (d) depict the computed total density of states (TDOS) and projected density of states (PDOS) for the adsorption of Li, Na, K, and Ca, respectively. There is a significant overlap at 0.70 eV below the Fermi level between the Ti 3*d* orbital and the Li 2*s* orbital, indicating *s*-*d* hybridization and therefore, strong binding of Li atoms on the Ti_3C_2 surface. Similarly for Na, K, and Ca, the *s*–

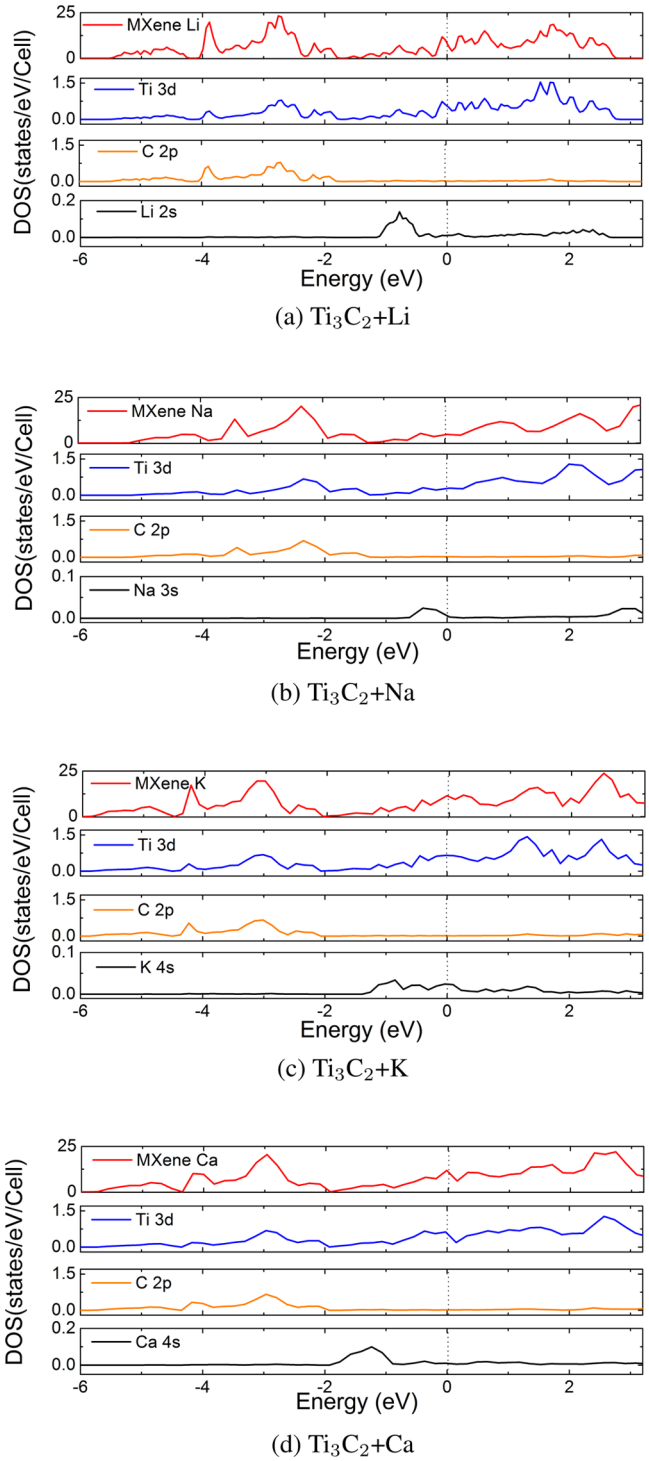

Figure 2. Total DOS and PDOS of Ti 3*d*, C 2*p*, and *s* orbitals of (a) Li, (b) Na, (c) K, and (d) Ca for the composite system of $Ti_3C_2M_{1/9}$. The Fermi levels are set to zero and are indicated by the dashed lines.

d hybridizations are also observed with peaks located at 0.33, 0.285, and 1.23 eV below the Fermi level, respectively.

To visualize the effect of adatom adsorption on the charge distribution, we calculated the bonding charge density which is obtained as the difference between the valence charge density before and after the bonding. Figure 3 shows the bonding charge density in the plane passing through both the adatom and the high symmetry line on the Ti_3C_2 monolayer. Red and blue colors indicate the electron accumulation and depletion,

dx.doi.org/10.1021/am501144q | ACS Appl. Mater. Interfaces 2014, 6, 11173–11179

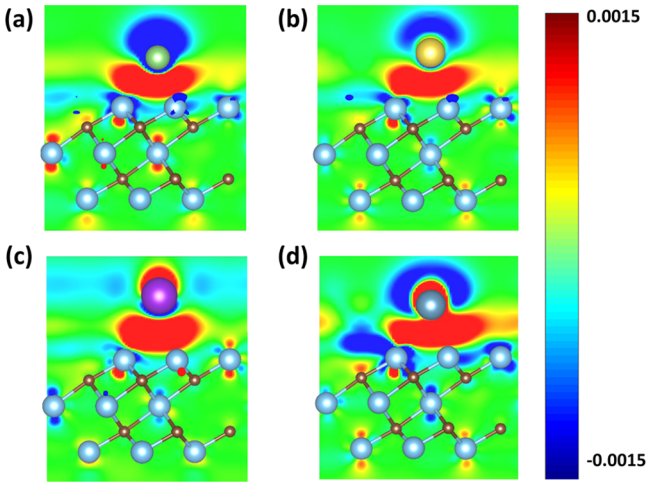

Figure 3. Bonding charge density for adatoms (a) Li, (b) Na, (c) K, and (d) Ca (being adsorbed at the *A* site) in $Ti_3C_2M_x$ system obtained as the charge density difference between the valence charge density before and after the bonding. Red and blue colors indicate the electron accumulation and depletion, respectively. The color scale is in the units of e/Bohr^3.

respectively. These bonding charge distributions clearly show the charge transfer from the adatoms to the Ti_3C_2 monolayer. The amount of charge transfer was estimated quantitatively by using Bader charge analysis and the results are presented in Table 1 for Li, Na, K, and Ca at energetically favored *A* and *B* sites. The Bader charge analysis is qualitatively consistent with our PDOS calculations. The area covered by the PDOS of valence s-states for Li is about 0.1 electrons, which indicates a charge transfer from Li to Ti_3C_2.

It is well-known that the diffusion barrier is a key factor that determines the rate at which a battery can be charged and discharged. We have investigated the diffusion barriers for Li, Na, K, and Ca in the Ti_3C_2 monolayer using the nudged elastic band (NEB) method[29] as implemented in VASP in order to evaluate the promise of Ti_3C_2 as high-rate electrode materials. The migration pathways are selected along the high symmetry line between energetically favorable adsorption sites on the surface and in Figure 4 we depict the optimized pathways. The calculated diffusion barrier for Li is 0.068 eV, in close comparison to the previously reported value.[23] For Na, K, and Ca, the diffusion barriers are 0.096, 0.103, and 0.118 eV, respectively. Compared to commercial anode materials based on TiO_2 polymorphs with a diffusion barrier about 0.35−0.65 eV for Li, Ti_3C_2 can exhibit faster transport and higher charge/discharge rate for Li, and even for other alkali elements. Another commercial anode material, graphite, needs to overcome a diffusion barrier larger than 0.3 eV for Li. This suggests that Ti_3C_2 is a promising candidate for high rate electrode materials.

3.3. Open Circuit Voltage and Theoretical Specific Capacity. In addition to the adsorption of single adatom on the Ti_3C_2 MXene, we also evaluated the OCVs as a function of the adatom concentration by varying x in the $Ti_3C_2M_x$ system.

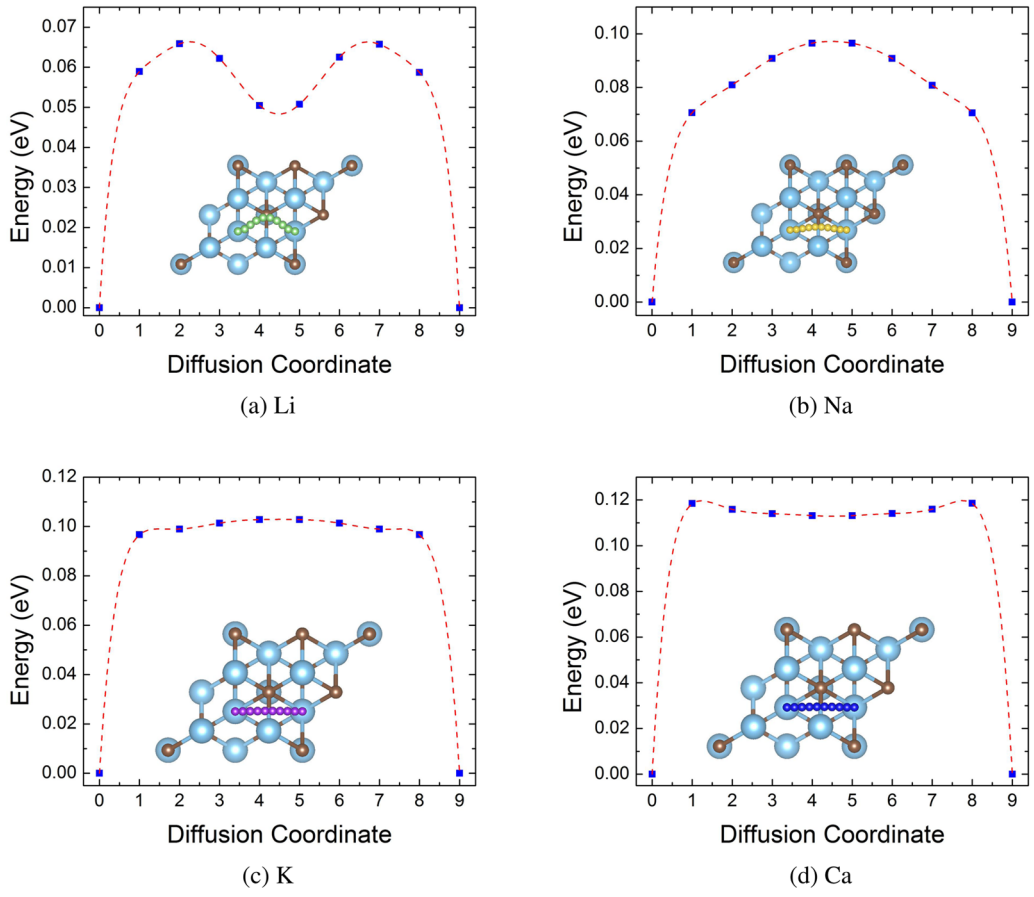

Figure 4. Schematic representation of the top view of the energetically optimized migration pathways and the corresponding diffusion barrier profiles of (a) Li, (b) Na, (c) K, and (d) Ca on Ti_3C_2 MXene.

We considered different x in the $Ti_3C_2M_x$ system, namely, 0.11, 0.25, 0.5, 0.75, and 1, by using different supercells with stoichiometry $(Ti_3C_2)_9M$, $(Ti_3C_2)_4M$, $(Ti_3C_2)_2M$, $(Ti_3C_2)_4M_3$ and Ti_3C_2M, respectively. Moreover, in order to determine whether adatoms can occupy other adsorption sites after fully covering the A sites of lowest adsorption energy, we computed the possibility of B sites adsorption by varying the number of adatoms in a 2 × 2 × 1 supercell from 1 to 4, corresponding to the adatom content x = 1.25, 1.5, 1.75, and 2.

In Figure 5, we depict the calculated OCVs as a function of the adatom concentration represented by x in the $Ti_3C_2M_x$

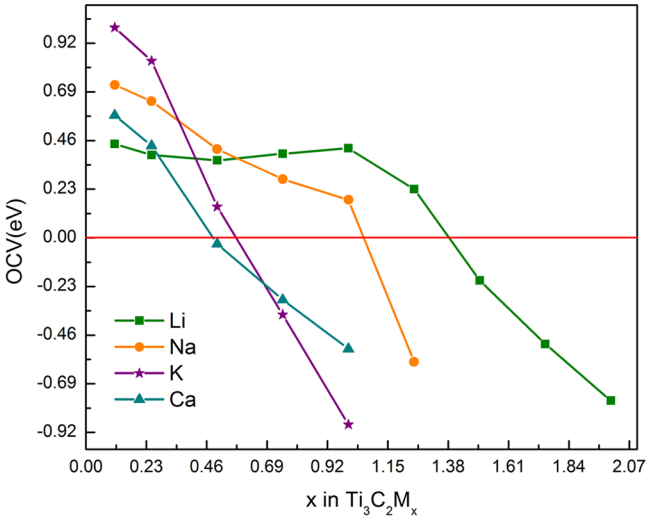

Figure 5. OCV changes with adatom content for the single-side adsorption of Li, Na, K, and Ca on the Ti_3C_2 surface. x < 1 corresponds to the adatom adsorption on the A site, and x > 1 corresponds to partial coverage of B sites and full coverage of A site. The x corresponding to zero OCV is used to estimate the maximum adatom content and capacity.

system. Only the highest OCV among different configurations is shown for each concentration. For all alkali elements studied herein except Li, the OCVs decrease with increased adatom concentration, but with different slopes. In Figure 5, OCVs of Na, K, and Ca decrease as x increases, while Li shows little sensitivity to the variance of x in the range $x \leq 1$. The OCV of Li starts to decrease when x > 1. Only A is shown in Figure 5 because the difference of OCVs between the A and B sites is less than 100 meV, which means one specific representation is enough for the trend. At low adatom content (x < 0.25), the OCVs of K, Na, Ca, and Li decrease; however, this trend changes at high adatom content (x > 0.8). The OCV of Li is now the highest, followed by Na, Ca, and K in that order. Once the OCV is zero, we reach a situation where no more adatoms can be adsorbed, which corresponds to the maximum x in $Ti_3C_2M_x$. Consequently, the capacity of each element on the Ti_3C_2 surface can be determined. For K and Ca, the estimated maximum x is approximately 0.6 and 0.5, respectively, meaning that the OCVs have dropped to zero before fully covering the A site. At x = 1, the OCVs of Li and Na are positive, indicating that additional adatoms can be adsorbed on the Ti_3C_2 surface where the A site is fully covered. For Li and Na, the maximum x is approximately 1.4 and 1.1 by assuming a linear relationship between two adatom contents around zero OCV. This result suggests that the Li and Na adatoms can seek other energetically favorable sites after fully covering the A site.

It is noted that the above discussion is based on the calculation assuming single-side adsorption. The fact that the charge transfer mainly occurs between the surface Ti(s) atoms and the adatom suggest the possibility of adsorption on double sides. In order to verify this, we considered a 2 × 2 × 1 supercell of Ti_3C_2 monolayer with increased adatom content on both surfaces. Our computations reveal that the 2 × 2 × 1 supercell of the Ti_3C_2 monolayer can accommodate up to 8 Li, 8 Na, 4 K, and 4 Ca adatoms, which corresponds to the chemical stoichiometry of $Ti_3C_2Li_2$, $Ti_3C_2Na_2$, Ti_3C_2K, and Ti_3C_2Ca with symmetric configuration of adatoms on both sides. The calculated OCVs are 0.413, 0.137, 0.128, and 0.087 eV, respectively. Therefore, we can estimate the maximum adatom content to be 2.8, 2.2, 1.2, and 1 for Li, Na, K, and Ca, respectively. For single-site adsorption, the maximum capacity C_M (mAh/g) can be computed from the maximum adatom content x_{max} as

$$C_M = \frac{1}{M_{Ti_3C_2}}[x_{max} \times z \times F \times 10^3] \quad (6)$$

where z is the valence number (z = 1 for Li, Na, and K; z = 2 for Ca), F is the Faraday constant (26.810 Ah/mol), and $M_{Ti_3C_2}$ is the atomic mass of Ti_3C_2 (167.62 g/mol). Based on the assumption of double-side adsorption, the theoretical capacities of Li, Na, K, and Ca on Ti_3C_2 MXene are calculated to be 447.8, 351.8, 191.8, and 319.8 mAh/g, respectively.

3.4. Effective Ionic Radius. As shown in Figure 5, the maximum coverage of adatoms on Ti_3C_2 monolayer vary with the alkali elements of different atomic numbers, which can be attributed to the effective size of the ionized adatom. For a given ion, the ionic radius is strongly dependent on the charge state. Therefore, an effective ionic radius $R^{\Delta q}$ can be defined as $R^{\Delta q} = R^0 + (R^1 - R^0)\Delta q$ by assuming a linear dependence on the charge state Δq with R^0 the atomic radius and R^1 the ionic radius of charge state +1. As shown in Table 2 the adsorbed Li,

Table 2. Relationship between Charge Transfer (Δq) and Effective Ionic Radius ($R^{\Delta q}$)[a]

	R^0 (Å)	R^1 (Å)	Δq (e$^-$)	$R^{\Delta q}$ (Å)
Li	1.55	0.68 (Li^+)	0.79	0.86
Na	1.90	0.97 (Na^+)	0.60	1.34
K	2.35	1.33 (K^+)	0.53	1.81
Ca	1.97	0.99 (Ca^{2+})	0.69	1.63

[a] $R^{\Delta q}$ is a linear interpolation of the atomic radius (R^0) and the ionic radius(R^1) of charge state +1.

Na, K, and Ca atoms are acting as electron donors and about 0.79, 0.60, 0.53, and 0.69 |e| are transferred from Li, Na, K, and Ca atoms to the Ti_3C_2 monolayer. The corresponding $R^{\Delta q}$ are 0.86, 1.34, 1.81, and 1.63 Å, respectively. The effective ionic radius is closely related to the maximum coverage of the alkali elements. For the full coverage of energetically favorable A sites, the distance between two nearest adatoms is 3.10 Å which indicates a critical radius 1.55 Å for the ionized adatoms. The $R^{\Delta q}$ of Li is much smaller than 1.55 Å, which is consistent with the fact that the OCVs are not sensitive to the coverage as indicated in Figure 5. For Na, the effective ionic radius is close to 1.55 Å, the coulomb repulsion between ionized adatoms leads to the reduced OCVs when increasing the coverage, but a full coverage of A sites can still be obtained. The fact that $R^{\Delta q}$ of K is greater than 1.55 Å makes the maximum adatom content x

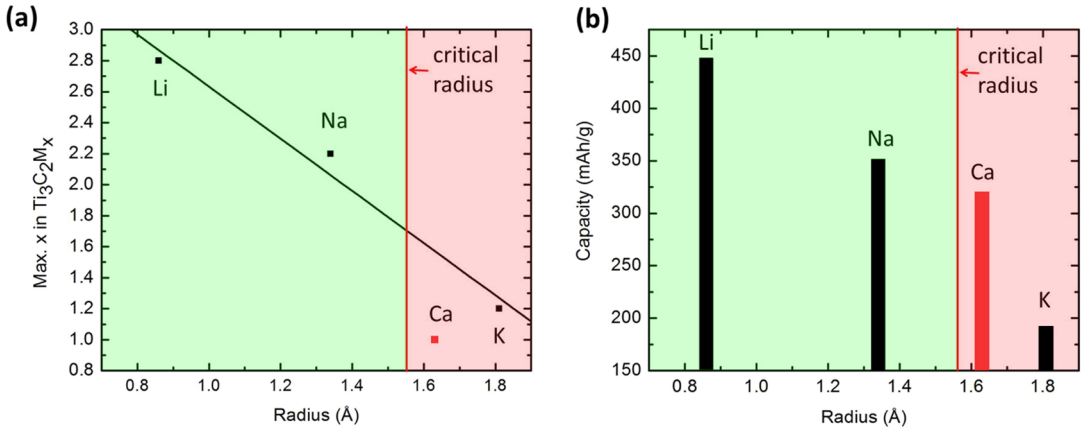

Figure 6. Relationship between (a) maximum adatom content (b) capacity and ionic radius for adsorption on both sides. The maximum adatom content and capacity of Li, Na, and K follow a linear relationship. Ca deviates from the linear expression due to its different valence electron structure.

$\sim$ 0.6. Although $R^{\Delta q}$ of Ca is smaller than that of K, the maximum x is only 0.5 due to the small OCV for low coverage.

We found that for Li, Na, and K a linear relationship between the effective ionic radius and the maximum adatom content x in $Ti_3C_2M_x$ can be established as

$$x_{max} = -1.68 \times R^{\Delta q} + 4.318 \quad (7)$$

in which x_{max} is calculated by taking into account the double-side adsorption. Care must be exercised that this relationship does not hold for Ca because Ca has two valence electrons which results in stronger interactions with the Ti_3C_2 monolayer. Correspondingly, we can establish a relationship between the capacity and the effective ionic radius by combining eqs 6 and 7

$$C_M = \frac{1}{M_{Ti_3C_2}}[(-1.68 \times R^{\Delta q} + 4.318) \times z \times F \times 10^3] \quad (8)$$

This expression provides a simple description for the theoretical capacity of alkali metals in terms of the effective ionic radius of the ionized adatoms. In Figure 6, we plot the calculated maximum adatom contents and capacities of $Ti_3C_2M_x$ as a function of effective ionic radius with Li, Na, K, and Ca adsorbed on two sides.

3.5. Comparison to Graphene. Our predicted high capacity of Ti_3C_2 MXene is in contrast to extensively studied graphene sheet. Although it displays various appealing properties, pristine single layered graphene is not a good candidate for electrode materials in LIBs.[30,31] For comparison, we performed the electronic structure calculations for pristine graphene with Li adatoms using a 2 × 2 × 1 supercell. Figure 7 shows the total DOS of graphene with a Li adatom, and the DOS projected onto C 2*p* and Li 2*s* orbitals. It can be seen that in the range 0–16 eV below the Fermi level, the C 2*p* orbital contributes most to the energy states. However, no significant peak of the Li 2*s* orbital below the Fermi level was observed. The peak of the Li 2*s* orbital occurs at 0.815 eV above the Fermi level, where there is an overlap of the peak of the C 2*p* orbital and the total DOS. This peak corresponds to an *s*-*p* antibonding orbital. Therefore, the lack of overlapped peaks below the Fermi level indicates the absence of hybridization of orbitals and therefore, a weaker bonding. As shown in Figure 2, an overlap of the Li 2*s* orbital with the Ti 3*d* orbital in Ti_3C_2 MXene occurs at 0.70 eV below

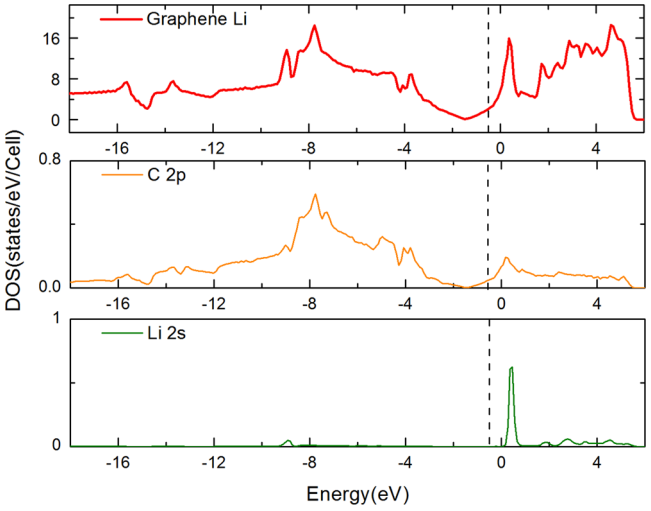

Figure 7. Total DOS of the pristine graphene with Li adatom and the PDOS onto C 2*p* and Li 2*s* orbitals.

the Fermi level. A significant and broad peak of Li overlaps with several peaks of the Ti 3*d* orbital, which indicates the existence of an *s*–*d* hybridization during Li adsorption.

4. CONCLUSION

With first-principles density functional method we investigated the electronic properties of the adsorption of Li, Na, K and Ca atoms on Ti_3C_2. Our results show a linear relationship between the effective ion radius, maximum adatom content, and capacities for alkali metals. Charge transfer determines the effective radius of ions, which plays a critical role during the metal-ion adsorption on the surface. Larger effective ionic radius enhances interaction between alkali atoms, thus lowering maximum adatom content and theoretical capacity of the alkali metals. Our calculated capacity values for Li, Na, K and Ca on Ti_3C_2 are 447.8, 351.8, 191.8, and 319.8 mAh/g, respectively. A simple expression to predict capacity by examining effective ionic radius is proposed here. Our results give insights for further experimental work in exploring and developing the potential of Ti_3C_2 for Li, Na, K, or Ca battery applications. It is noteworthy that Ti_3C_2 is only one member of the MXene family. This suggests the need for further experimental and

computational investigations on MXenes as promising electrode materials for energy storage applications.

AUTHOR INFORMATION

Corresponding Author

*E-mail: vshenoy@seas.upenn.edu.

Notes

The authors declare no competing financial interest.

ACKNOWLEDGMENTS

D.E., J.L., and V.B.S. gratefully acknowledge the support of the Army Research Office through Contract W911NF-11-1-0171. The work done at Drexel University was supported by the Assistant Secretary for Energy Efficiency and Renewable Energy, Office of Vehicle Technologies of the U.S. Department of Energy under Contract No. DE-AC02-05CH11231, subcontract No. 6951370, under the Batteries for Advanced Transportation Technologies (BATT) Program. The authors would like to thank Dr. Michel Barsoum for his constructive comments and helpful discussions.

REFERENCES

(1) Dunn, B.; Kamath, H.; Tarascon, J.-M. Electrical Energy Storage for the Grid: A Battery of Choices. *Science* **2011**, *334*, 928−935.

(2) Chen, H.; Cong, T. N.; Yang, W.; Tan, C.; Li, Y.; Ding, Y. Progress in Electrical Energy Storage System: A Critical Review. *Prog. Nat. Sci.* **2009**, *19*, 291−312.

(3) Goodenough, J. B.; Kim, Y. Challenges for Rechargeable Li Batteries. *Chem. Mater.* **2009**, *22*, 587−603.

(4) Slater, M. D.; Kim, D.; Lee, E.; Johnson, C. S. Sodium-Ion Batteries. *Adv. Funct. Mater.* **2013**, *23*, 947−958.

(5) Pan, H.; Hu, Y.-S.; Chen, L. Room-Temperature Stationary Sodium-Ion Batteries for Large-Scale Electric Energy Storage. *Energy Environ. Sci.* **2013**, *6*, 2338−2360.

(6) Eftekhari, A. Potassium Secondary Cell Based on Prussian Blue Cathode. *J. Power Sources* **2004**, *126*, 221−228.

(7) DiVincenzo, D. P.; Mele, E. J. Cohesion and Structure in Stage-1 Graphite Intercalation Compounds. *Phys. Rev. B* **1985**, *32*, 2538−2553.

(8) Liu, J.; Liu, X.-W. Two-Dimensional Nanoarchitectures for Lithium Storage. *Adv. Mater.* **2012**, *24*, 4097−4111.

(9) Naguib, M.; Mashtalir, O.; Carle, J.; Presser, V.; Lu, J.; Hultman, L.; Gogotsi, Y.; Barsoum, M. W. Two-Dimensional Transition Metal Carbides. *ACS Nano* **2012**, *6*, 1322−1331.

(10) Naguib, M.; Kurtoglu, M.; Presser, V.; Lu, J.; Niu, J.; Heon, M.; Hultman, L.; Gogotsi, Y.; Barsoum, M. W. Two-Dimensional Nanocrystals: Two-Dimensional Nanocrystals Produced by Exfoliation of Ti_3AlC_2. *Adv. Mater.* **2011**, *23*, 4248−4253.

(11) Barsoum, M. W. The $M_{N+1}AX_N$ Phases: A New Class of Solids; Thermodynamically Stable Nanolaminates. *Prog. Solid State Chem.* **2000**, *28*, 201−281.

(12) Naguib, M.; Halim, J.; Lu, J.; Cook, K. M.; Hultman, L.; Gogotsi, Y.; Barsoum, M. W. New Two-Dimensional Niobium and Vanadium Carbides as Promising Materials for Li-Ion Batteries. *J. Am. Chem. Soc.* **2013**, *135*, 15966−15969.

(13) Shein, I.; Ivanovskii, A. Planar Nano-Block Structures $Ti_{n+1}Al_{0.5}C_n$ and $Ti_{n+1}C_n$ (n = 1 and 2) from MAX Phases: Structural, Electronic Properties and Relative Stability from First Principles Calculations. *Superlattices Microstruct.* **2012**, *52*, 147−157.

(14) Shein, I.; Ivanovskii, A. Graphene-Like Titanium Carbides and Nitrides $Ti_{n+1}C_n$, $Ti_{n+1}N_n$ (n = 1, 2, and 3) from De-Intercalated MAX Phases: First-Principles Probing of Their Structural, Electronic Properties and Relative Stability. *Comput. Mater. Sci.* **2012**, *65*, 104−114.

(15) Lane, N. J.; Vogel, S. C.; Caspi, E. N.; Barsoum, M. W. High-Temperature Neutron Diffraction and First-Principles Study of Temperature-Dependent Crystal Structures and Atomic Vibrations in Ti_3AlC_2, Ti_2AlC, and $Ti_5Al_2C_3$. *J. Appl. Phys.* **2013**, *113*, No. 183519.

(16) Lukatskaya, M. R.; Mashtalir, O.; Ren, C. E.; DallAgnese, Y.; Rozier, P.; Taberna, P. L.; Naguib, M.; Simon, P.; Barsoum, M. W.; Gogotsi, Y. Cation Intercalation and High Volumetric Capacitance of Two-Dimensional Titanium Carbide. *Science* **2013**, *341*, 1502−1505.

(17) Khazaei, M.; Arai, M.; Sasaki, T.; Chung, C.-Y.; Venkataramanan, N. S.; Estili, M.; Sakka, Y.; Kawazoe, Y. Novel Electronic and Magnetic Properties of Two-Dimensional Transition Metal Carbides and Nitrides. *Adv. Funct. Mater.* **2013**, *23*, 2185−2192.

(18) Xie, Y.; Kent, P. Hybrid Density Functional Study of Structural and Electronic Properties of Functionalized Ti $_{n+1}X_n$ (X = C, N) monolayers. *Phys. Rev. B* **2013**, *87*, No. 235441.

(19) Kurtoglu, M.; Naguib, M.; Gogotsi, Y.; Barsoum, M. W. First Principles Study of Two-Dimensional Early Transition Metal Carbides. *MRS Commun.* **2012**, *2*, 133−137.

(20) Naguib, M.; Come, J.; Dyatkin, B.; Presser, V.; Taberna, P.-L.; Simon, P.; Barsoum, M. W.; Gogotsi, Y. MXene: A Promising Transition Metal Carbide Anode for Lithium-Ion Batteries. *Electrochem. Commun.* **2012**, *16*, 61−64.

(21) Mashtalir, O.; Naguib, M.; Mochalin, V. N.; Dall Agnese, Y.; Heon, M.; Barsoum, M. W.; Gogotsi, Y. Intercalation and Delamination of Layered Carbides and Carbonitrides. *Nat. Commun.* **2013**, *4*, 1716.

(22) Come, J.; Naguib, M.; Rozier, P.; Barsoum, M.; Gogotsi, Y.; Taberna, P.-L.; Morcrette, M.; Simon, P. A Non-Aqueous Asymmetric Cell with a Ti_2C-Based Two-Dimensional Negative Electrode. *J. Electrochem. Soc.* **2012**, *159*, A1368−A1373.

(23) Tang, Q.; Zhou, Z.; Shen, P. Are MXenes Promising Anode Materials for Li Ion Batteries? Computational Studies on Electronic Properties and Li Storage Capability of Ti_3C_2 and $Ti_3C_2X_2$ (X = F, OH) Monolayer. *J. Am. Chem. Soc.* **2012**, *134*, 16909−16916.

(24) Kresse, G.; Hafner, J. Ab Initio Molecular Dynamics for Liquid Metals. *Phys. Rev. B* **1993**, *47*, 558−561.

(25) Kresse, G.; Furthmüller, J. Efficient Iterative Schemes for Ab Initio Total-Energy Calculations Using a Plane-Wave Basis Set. *Phys. Rev. B* **1996**, *54*, 11169−11186.

(26) Blöchl, P. E. Projector Augmented-Wave Method. *Phys. Rev. B* **1994**, *50*, 17953−17979.

(27) Perdew, J. P.; Burke, K.; Ernzerhof, M. Generalized Gradient Approximation Made Simple. *Phys. Rev. Lett.* **1996**, *77*, 3865−3868.

(28) Aydinol, M. K.; Kohan, A. F.; Ceder, G.; Cho, K.; Joannopoulos, J. Ab Initio Study of Lithium Intercalation in Metal Oxides and Metal Dichalcogenides. *Phys. Rev. B* **1997**, *56*, 1354−1365.

(29) Mills, G.; Jónsson, H.; Schenter, G. K. Reversible Work Transition State Theory: Application to Dissociative Adsorption of Hydrogen. *Surf. Sci.* **1995**, *324*, 305−337.

(30) Chan, K. T.; Neaton, J. B.; Cohen, M. L. First-Principles Study of Metal Adatom Adsorption on Graphene. *Phys. Rev. B* **2008**, *77*, No. 235430.

(31) Lee, E.; Persson, K. A. Li Absorption and Intercalation in Single Layer Graphene and Few Layer Graphene by First Principles. *Nano Lett.* **2012**, *12*, 4624−4628.